Sensors and Actuators A 190 (2013) 66–76

Contents lists available at SciVerse ScienceDirect

Sensors and Actuators A: Physical

journal homepage: www.elsevier.com/locate/sna

Control, navigation and collision avoidance for an unmanned aerial vehicle

K.Y. Chee, Z.W. Zhong*

School of Mechanical and Aerospace Engineering, Nanyang Technological University, 50 Nanyang Avenue, Singapore 639798, Republic of Singapore

ARTICLE INFO

Article history:
Received 20 May 2012
Received in revised form 29 August 2012
Accepted 11 November 2012
Available online 23 November 2012

Keywords:
Unmanned aerial vehicle
Infra-red sensor
Ultrasonic sensor
Barometer
Pressure sensor
Collision avoidance

ABSTRACT

This article reports the development of an unmanned aerial vehicle capable of attitude estimation and stabilization through the implementation of a nonlinear complementary filter and proportional-integral rate controllers. Four infra-red sensors and an ultrasonic sensor are integrated with the main platform for the collision avoidance schemes and for altitude control, respectively. Critical mission capabilities for the vehicle such as altitude hold and collision avoidance are developed. An outdoor navigation scheme and collision avoidance algorithms are also proposed to enhance the vehicle autonomy. Experimental results have shown that the implemented attitude and altitude controllers are effective and the platform is capable of navigating autonomously with user-defined waypoints. The collision avoidance algorithms allow the platform to avoid obstacles, both reactively and in the midst of navigation routines.

1. Introduction

In recent decades, unmanned aerial vehicles (UAVs) have been utilized extensively in many military and civil missions. Some of these missions include search and rescue operations, aerial surveillance and sensing applications. Due to the high level of autonomy in these platforms, the success rate of these missions with such UAVs can be exceptional and at the same time, their usage promotes safety as human lives are not endangered. Another advantage that these unmanned platforms have is the ability to achieve stealth more readily than manned aircraft, due to their relatively smaller sizes and propulsion systems used. With this ability, many of the military missions, such as payload/weaponry drop-offs and reconnaissance can be executed without detection from enemy units. Among these existing UAVs, the quadrotor helicopter stands out as a versatile type of rotary wing vehicle and it is capable of executing tasks and missions that are too difficult or dangerous for manned vehicles to undertake.

The design and development of quadrotor platforms have gained popularity in recent years, due to their flexibility and potential capabilities. Considerable work has been done to investigate aerodynamic factors in hope of enhancing vehicle performance and efficiency. Some of these factors include the distortion and disruption of airflow due to the flow interaction between the four rotating blades at close proximity and propeller blade flapping [1,2]. Airfoil and platform designs can also be customized in order to improve aerodynamic efficiency [1].

The flight dynamics of a quadcopter is complex and this makes attitude and position estimation as well as controller implementation challenging. There have been several attempts to model the quadrotor helicopter in order to comprehend its dynamics [3,4]. Numerous controllers, both linear and nonlinear, have been proposed to allow the platform to achieve a high level of stability [5–9]. Examples include model reference adaptive control [7] [7], a nonlinear controller derived using back-stepping approaches [8] and a controller based on a nested saturation technique [9]. There is also a considerable body of work on estimating attitude for onboard flight control systems [10–12]. Apart from attitude estimation and stabilization, work has been done to expand the capabilities of the platforms. Altitude control is seen as essential for many applications and thus, it has been investigated and some significant studies on it can be found [13–15]. Autonomous navigation and collision avoidance algorithms are useful in enhancing the system autonomy. Various methods such as two-dimensional laser mapping, optical approaches and reactive infra-red sensing have been introduced to achieve satisfactory indoor navigation and collision avoidance [16–18]. Some aerial vehicles saw success with outdoor navigation with the use of the Global Positioning System (GPS) devices [19,20].

In this work, an unmanned quadrotor aerial vehicle capable of attitude estimation and stabilization through the implementation of a nonlinear complementary filter and proportional-integral rate controllers is developed. Four infra-red sensors and an ultrasonic sensor are integrated with the main platform for the collision avoidance schemes and for altitude control respectively. Critical mission

* Corresponding author. Tel.: +65 6790 5588; fax: +65 6791 1859.
E-mail address: mzwzhong@ntu.edu.sg (Z.W. Zhong).

0924-4247/$ – see front matter © 2012 Elsevier B.V. All rights reserved.
http://dx.doi.org/10.1016/j.sna.2012.11.017

Nomenclature

α_m	Measurement vector of 3-axes accelerometer
β	Intermediate controller output of attitude controller
ξ_b, ξ_s	Weights given to barometer and ultrasonic sensor altitude measurements, respectively
μ_m	Measurement vector of 3-axes magnetometer
Ω	Measurement vector of 3-axes gyroscope
ω_u	Output of attitude controller
ω_u	Output of altitude proportional-integral-derivative controller
ϕ, θ, ψ	Roll, pitch and yaw Euler angles of vehicle
b	Gyroscope measurement bias
e	Control error of nonlinear complementary filter
K_P, K_I, K_D	Proportional, integral, and derivative gains of a PID controller
$K_{P,rate}$	Proportional rate gain of the attitude controller
R_B^I	Transformation matrix from vehicle body axes to inertial axes
$R_{B,x}^I$	First column of the transformation matrix from vehicle body axes to inertial axes
$R_{B,z}^I$	Third row of the transformation matrix from vehicle body axes to inertial axes
$\dot{R}_B^I$	Rate of transformation matrix from vehicle body axes to inertial axes
x, y, z	Position estimates of vehicle
x_d, y_d, z_d	Desired positions of vehicle
$()_x$	Vector operator to transform a cross-product into a skew symmetric matrix

Subscript

e	Of the nonlinear complementary filter for attitude estimation
ca	Of controllers in collision avoidance schemes

capabilities for the vehicle such as altitude hold and collision avoidance are developed. An outdoor navigation scheme and collision avoidance algorithms are also proposed to enhance the vehicle autonomy.

In this article, section 2 deals with the development of the platform which includes the structure, flight controller and external sensors used onboard. Section 3 elaborates on the implementation of the algorithms that are used for attitude and altitude control, autonomous navigation and for the collision avoidance schemes. Flight test results and their discussions are given in section 4 and a conclusion is drawn in section 5.

2. Platform preliminaries

The quadrotor platform was developed through the integration of different mechanical and electrical components. Fig. 1 illustrates the complete system with the structural frame, propulsion system, external sensors as well as the autopilot and flight processor unit, while Fig. 2 depicts the operation flow diagram of the system. The inertial measurement unit (IMU), together with the magnetometer, provides the platform with a complete nine degrees-of-freedom attitude and heading reference system (AHRS), which serves as a prerequisite for the control and navigation algorithms. The GPS module provides position estimates which are used in the autonomous navigation algorithm, while the infra-red (IR) sensors provide measurements for obstacle detection. Details of the various components are elaborated in the following sections.

Fig. 1. Integrated quadrotor platform with flight controller, sensors and propulsion.

2.1. Structural frame

The arms and centre plates of the quadrotor frame are made using carbon fiber. Connections between the centre plates and arms, as well as the motor mounts are made of aluminum. The modular integration of the frame allows components to be replaced easily if necessary. The frame, illustrated in Fig. 3, is 485 cm long from motor to motor and weighs approximately 450 g. The propulsion system is mounted directly onto this frame.

2.2. Propulsion system

The propulsion unit for the quadrotor platform consists of four 950-kV brushless DC motors and four electronic speed controllers which can take up to 18 A of current during flight operations. The power source for the system is a 3-cell lithium polymer battery. Propellers mounted on the motors are of 10 inches length and have a fixed pitch angle of 4.5 degrees. This propulsion configuration allows safe operations of the platform and ensures excellent lift and thrust performance for all of the flight tests.

2.3. Flight processor and AHRS

For onboard processing and operations of the implemented algorithms, a 16-MHz Atmega 2560 embedded processor is used for the platform. An inertial measurement unit (IMU) shield, which consists of 3-axes accelerometers (Analog Devices ADX330) and gyroscopes (Invensense IDG500), is integrated with the flight processor. The shield also consists of a 16-MB data logger that is used for storage of flight data. It also has analog ports, as well as serial and I2C interfaces, which are necessary for the integration of external sensors. A magnetometer (Honeywell HMC5883L) is connected to the IMU shield through an I2C port and that completes the AHRS for the platform. The magnetometer is read using an I2C interface found on the IMU shield.

2.4. External sensors and range finders

Four infra-red sensors (Sharp GP2Y0A02YK0F) and an ultrasonic sensor (MaxBotix LV-EZ0), illustrated in Fig. 4, are integrated with the main platform for the collision avoidance schemes and for altitude control respectively. The IR sensors have a maximum range of 1.5 m, while the ultrasonic sensor can sense objects up to 6.45 m. Measurements from these range finders are read through analog ports available on the IMU shield. The GPS module used for

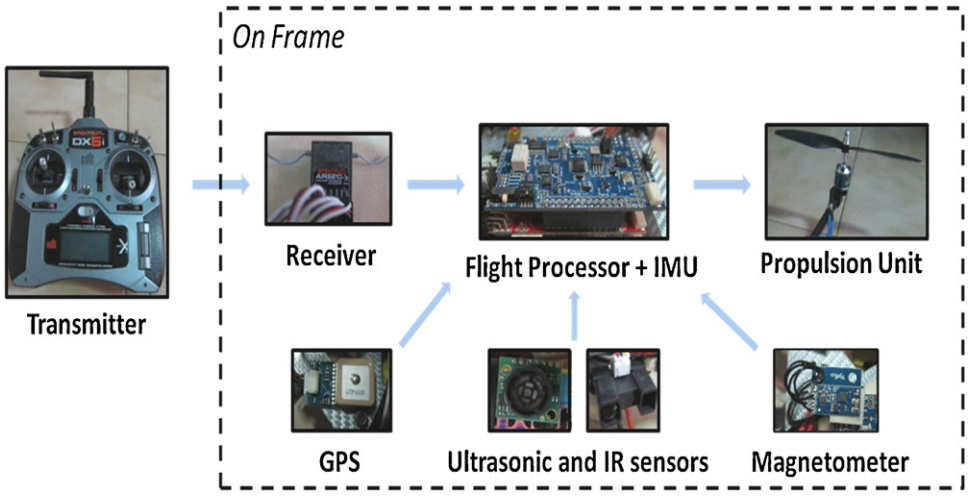

Fig. 2. The operation flow diagram of the system.

Fig. 3. Empty frame of the quadrotor platform.

navigation purposes is the MediaTek MT3329 unit and it is connected through a serial connection to the flight processor. The sensors mentioned above were mainly chosen based on their weight and their adaptability for connection to the flight processor. The ultrasonic sensor weighs approximately 5 g and has dimensions of 2 cm by 2 cm by 1.5 cm. The infra-red sensors weigh 4.8 g and have dimensions of 4 cm by 1 cm by 2.2 cm.

3. Algorithm development

3.1. Attitude estimation and control architecture

A nonlinear complementary filter was implemented for attitude estimation. The main tool utilized for this implementation is a transformation matrix between an inertial frame

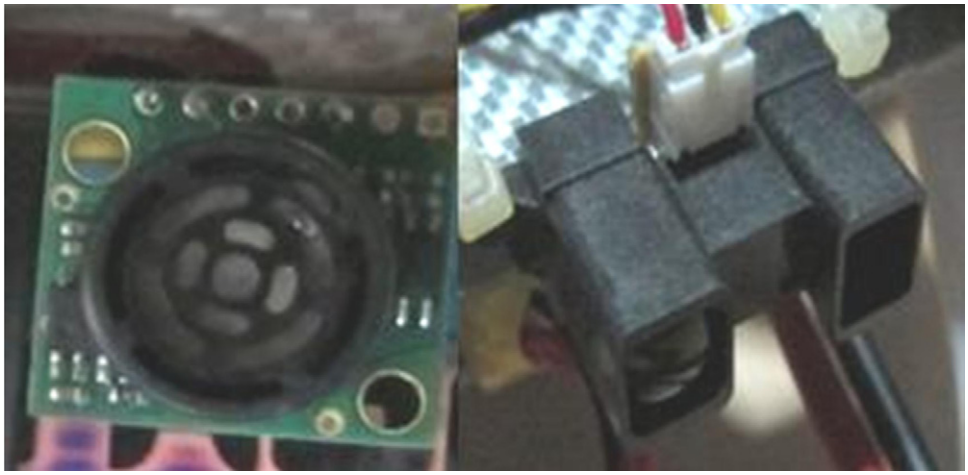

Fig. 4. Ultrasonic and infra-red range finders used.

of reference and the body axes of the vehicle, using Euler angles [21]:

$$R_B^I = \begin{bmatrix} \cos\theta\cos\psi & \sin\phi\sin\theta\cos\psi - \cos\phi\sin\psi & \cos\phi\sin\theta\cos\psi + \sin\phi\sin\psi \\ \cos\theta\sin\psi & \sin\phi\sin\theta\sin\psi + \cos\phi\sin\psi & \cos\phi\sin\theta\sin\psi - \sin\phi\cos\psi \\ -\sin\theta & \sin\phi\cos\theta & \cos\phi\cos\theta \end{bmatrix} \quad (1)$$

Because this transformation matrix propagates through time, the attitude of the vehicle is extracted from elements of the matrix. Orthogonality of the matrix is maintained by incorporating the orthogonal error equally into the deviated row vectors in the matrix. Gyroscope bias exists for all strap-down inertial navigation systems and this filter corrects the bias through the implementation of an estimation feedback loop [21]:

$$\dot{R}_B^I = R_B^I(\Omega - b + K_{P,e}e)_x \quad (2)$$

$$b = -K_{I,e}e \quad (3)$$

$$e = (R_{B,z}^I)_x\alpha_m + R_I^B((R_{B,x}^I)_x\mu_m) \quad (4)$$

Proportional-integral controllers were implemented to stabilize the platform in the rolling, pitching and yawing axes. The rate input to the controllers can be seen as the inner loop while the proportional and integral terms are components of the outer loop for the controllers. These attitude controllers can be formulated in the following expressions:

$$\beta = K_P(u - u_d) + K_I\int(u - u_d) \quad (5)$$

$$\omega_u = K_{P,rate}(\beta - \dot{u}) \quad (6)$$

where u and u_d are the estimated and desired attitude variables (ϕ, θ, or ψ) respectively and $\dot{u}$ is the rate of the attitude variable.

3.2. Altitude control scheme

The estimation of the altitude is done through the usage of a barometer and an ultrasonic sensor. Measurements from these sensors were integrated using a weighting scheme [22], based on the reliability of the sensors at different altitudes. The scheme can be represented by the following piece-wise function:

$$\xi_b = \begin{cases} 0 & \text{if } z_s < z_{\min} \\ 1 & \text{if } z_s > z_{\max} \\ \dfrac{z_s - z_{\min}}{z_{\max} - z_{\min}} & \text{, otherwise.} \end{cases} \quad (7)$$

$$\xi_s = 1 - \xi_b \quad (8)$$

where z_{min} and z_{max} represent the range in which the barometer and ultrasonic sensor measurements are weighted.

For regulating the error dynamics of the altitude, a proportional-integral-derivative controller was developed. Different gains were utilized for different altitude segments and they can be seen as a form of gain scheduling. The controller can be expressed as:

$$\omega_z = K_{P,z}(z - z_d) + K_{I,z}\int(z - z_d) + K_{D,z}\frac{d(z - z_d)}{dt} \quad (9)$$

where z_d and z are the desired and estimated altitudes of the vehicle respectively. The output from this controller generates a throttle command and that regulates the altitude of the vehicle.

3.3. Autonomous navigation

An Autonomous navigation algorithm is proposed to allow the platform to move between user-defined waypoints, as shown in Fig. 5. First, the position of the vehicle is estimated using the GPS unit, which has a constant update rate of 10 Hz. Besides travelling sequentially from one waypoint to another, the bearing of the vehicle is also kept close to that of the next waypoint in order to reduce cross-track error during motion. The vehicle is also commanded to loiter in between waypoint transitions for a user-defined period of time. The navigation scheme is governed by two proportional-integral-derivative controllers which take in the errors between the latitude and longitude of the current and targeted positions, similar to the one shown in Equation 9. The controller outputs are translated from the navigation to the body axes through a conventional transformation matrix.

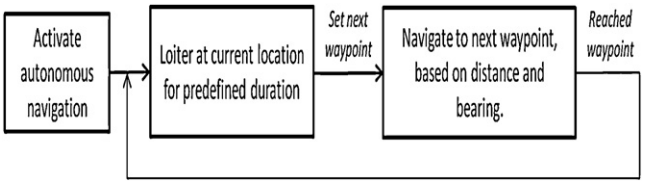

Fig. 5. Autonomous navigation scheme.

3.4. Collision avoidance algorithm

The first of the two collision avoidance schemes is a reactive quad-directional algorithm which allows the vehicle to avoid obstacles that are in its vicinity [22]. Measurements from the infrared sensors, which are mounted at the four edges of the central plate of the platform, are paired and compared against for obstacle detection, because the positions of these sensors are known prior to flight. For instance, when an obstacle is detected 1 meter in front of the platform via the frontal IR sensor, there exists a difference in measurements between the front and back IR sensors, and this is formulated as a distance error. It is then used as a feedback error in the closed loop position controllers, and attitude commands are given to allow the vehicle to shift away from the obstacle. Once the distance between the platform and the obstacle is farther than the safety distance set by the user, which is in this case the maximum range of the IR sensor, the algorithm ceases the collision avoidance commands and allows the vehicle to operate freely. The case where the obstacle is detected from either of the sides is analogous to the above-mentioned example. A pair of collision avoidance attitude controllers is implemented to regulate the distance between the vehicle and potential obstacles. They generate roll and pitch commands to avoid the obstacles and can be expressed as:

$$\phi_{ca} = K_{P,ca}(y - y_d) + K_{I,ca}(y - y_d) + K_{D,ca}\frac{d(y - y_d)}{dt} \quad (10)$$

$$\theta_{ca} = K_{P,ca}(x - x_d) + K_{I,ca}(x - x_d) + K_{D,ca}\frac{d(x - x_d)}{dt} \quad (11)$$

The second collision avoidance scheme is one, which is modified from the first and is integrated with the navigation algorithm. Besides avoiding obstacles reactively, an additional command is given to the vehicle for it to generate an obstacle-free path by moving backward and sideward, away from the object concurrently. Upon detection of the obstacle in any particular direction, commands will be sent to the platform to allow it to re-position itself away from the object, based on the measurements from the IR sensors. This is made possible due to the non-holonomic properties of the quadrotor platform, and thus there is no turn radius constraint for the platform. These motion commands are repeated until the object is no longer detected by any of the IR sensors. This allows the vehicle to avoid any obstacle of unknown shape and size. During the activation of this scheme, the navigation

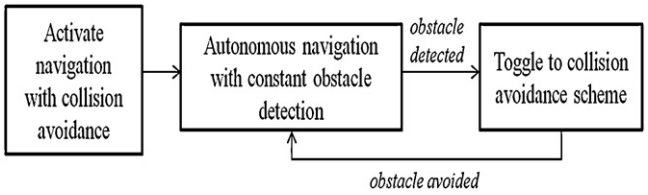

Fig. 6. Scheme for navigational collision avoidance.

commands are temporarily re-scheduled. Fig. 6 illustrates this combinational scheme of autonomous navigation with collision avoidance.

These schemes implemented for the quadrotor platform are summarized in the schematic diagram shown in Fig. 7. The primary loop shown in the figure is responsible for the basic operation and controls of the platform, and it is running at approximately 200 Hz. The attitude stabilization algorithm and attitude measurements can be found in this loop. The secondary loop, which is running at approximately 50 Hz, incorporates the algorithms required for the altitude control, navigation and collision avoidance routines. Measurements from the GPS module, magnetometer, ultrasonic and IR sensors are used in this secondary loop as well.

4. Flight test results and discussion

4.1. Attitude estimation and stabilization

First, ground tests were conducted to verify the estimation algorithm, by inducing static and dynamic motions on the IMU and flight processor. The nonlinear complementary filter performed well during the ground tests. Fig. 8 depicts the pitch angle estimates given by the nonlinear complementary filter during one of the AHRS simulations. In this series of tests, the AHRS was put into motion to validate the accuracy of the algorithm. The pitch angle estimate derived directly from the gyroscope was drifting at a rate of approximately 0.35°/s. This drift rate is unacceptable for most flight applications, with a minimum operating time of approximately 10 minutes. Although the accelerometer angle estimate was not drifting, it was generally noisy and thus it could not be used as well.

As shown in the figure, it was able to eliminate the drifting effects caused by the gyroscope and at the same time obtain a set of noise-free measurements as compared to those of the accelerometers. The filter was capable of estimating the attitude during both static and dynamic simulations of the AHRS module, proving its robustness for flight implementation. Although there is an initial settling time of approximately 6 seconds for this filter, this is

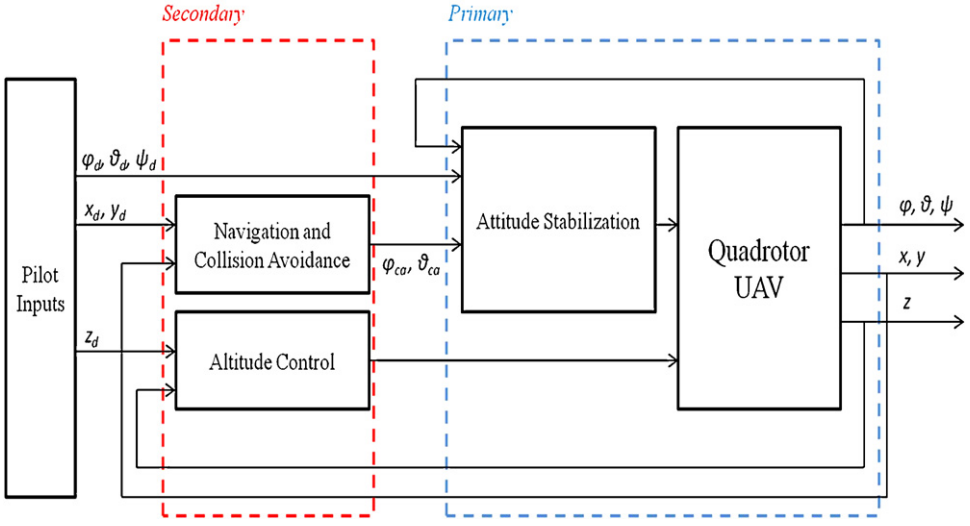

Fig. 7. Schematic diagram for algorithm implementation.

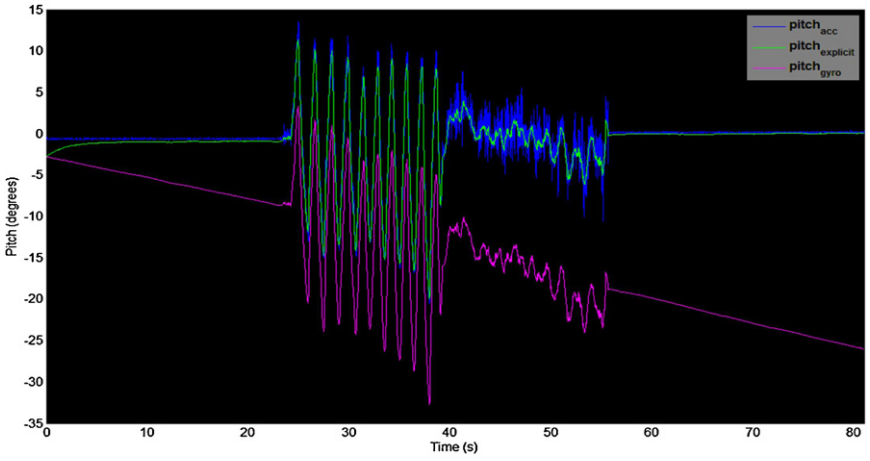

Fig. 8. Attitude estimates from nonlinear complementary filter.

Fig. 9. Flight tests for the verification of attitude estimation and stabilization.

not significant for the operation of the vehicle. The roll and yaw angles were also estimated from this filter and similar results were obtained.

Flight tests of the attitude estimation and stabilization algorithms were conducted in appropriate indoor and outdoor environments. As shown in the left frame of Fig. 9, the platform, highlighted in red, was flown approximately 5 meters above the ground in an outdoor flight, when wind conditions were not strong enough to cause major disturbances to the platform. In some of the subsequent trials, the performance of the UAV was tested against mild gust disturbances. For the indoor flights, the platform was flown at approximately 1 meter above the ground, as shown in the right frame of Fig. 9. These tests aided in the verification of the above-mentioned algorithms, without gust disturbances.

For flight testing of the attitude estimation algorithm, the platform was kept at a near-hover state during flight. Data logging was conducted to collect the information on the angles estimates based on the nonlinear complementary filter. The pitch angle estimates shown in Fig. 10 demonstrate the capability of the nonlinear complementary filter during flight. It was able to attenuate the high level of noise present in the accelerometer measurements, even when the accelerometer noise was much higher as compared to AHRS simulations. The noise is due to the vibrations induced by the motors and those were transferred to the flight controller through the structural frame of the vehicle. In general, the filter provided excellent attitude estimation abilities, which is a pre-requisite for the attitude stabilization algorithm.

In order to test the implemented attitude control architecture, flight tests were performed to observe the dynamic responses of the quadrotor UAV. During these flight tests, the gains for the attitude control loops were optimized to obtain good platform stability.

Fig. 11 depicts the errors of the roll and pitch angle estimates during one of the flight tests. As shown, the errors were regulated reasonably well during flight and this allowed good matching and tracking between the desired and estimated angles. With that, the platform was stabilized and other tasks such as altitude control, autonomous navigation and collision avoidance can be performed.

4.2. Altitude control results

The altitude control flight trials were conducted in various environments and at different altitudes to verify the robustness of the sensor, against different surfaces and the noise properties. One of these tests is shown in Fig. 12. The platform was flown in an indoor test-bed and was commanded to maintain altitude control. At the same time, the true altitude of the platform was measured using an external measuring device. For this example shown in Fig. 12, the true altitude of the platform is approximately 1 meter.

Tests and results for the altitude estimation and control algorithm can be illustrated using three sub-schemes, namely the pressure sensor, ultrasonic sensor and fusion sub-schemes.

First, by implementing the ultrasonic sensor sub-scheme, the tests were conducted at varying altitudes, and the error plots

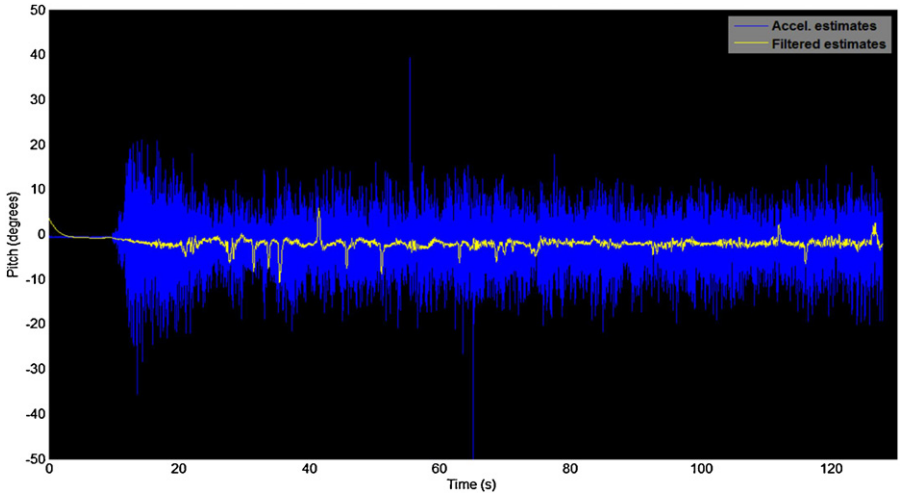

Fig. 10. Attitude estimates during flight test.

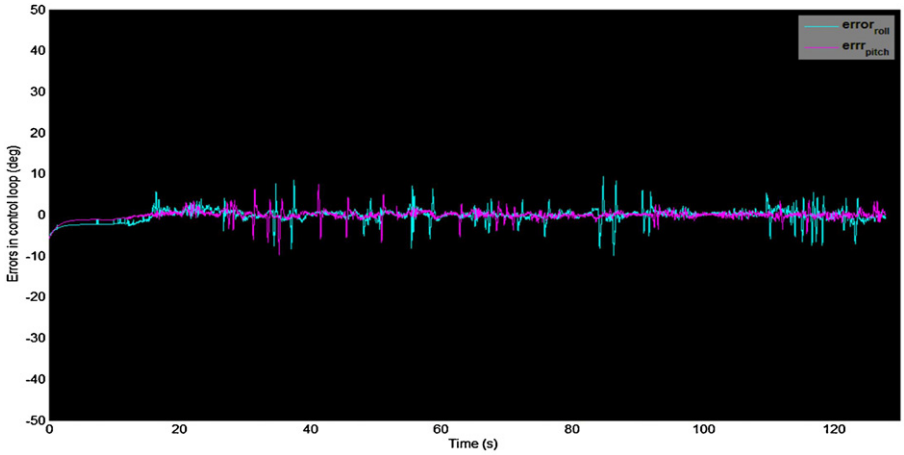

Fig. 11. Attitude errors for attitude controllers.

Fig. 12. Flight tests for the verification of altitude estimation and control algorithms.

of the altitudes are shown in Fig. 13. At lower altitudes, it can be observed from the magenta plot that altitude tracking was accurate and the standard deviation of the error was 0.0762 m.

At mid and higher altitudes (green and blue plots respectively), the ultrasonic sensor readings were fairly noisy but the platform was still able to maintain its altitude with standard deviations of 0.291 m and 0.522 m respectively.

Next, the altitude controller was tested with the pressure sensor sub-scheme. It was also tested at different altitudes, and the results are plotted in Fig. 14. As illustrated in the figure, the pressure sensor altitude errors generally had a range of 1.5 m and an average standard deviation of 0.556 m, but they were less noisy as compared to the ultrasonic sensor measurements as they have been filtered. Although they cannot predict altitudes to a high precision, they are useful as approximations when the platform is at higher altitudes, where ultrasonic sensor measurements are not available or when the ultrasonic sensors readings are noisy.

The third fusion sub-scheme is altitude tracking and control using a combined weighted altitude from both the pressure sensor and ultrasonic sensor readings. These tests were also performed at different heights, and Fig. 15 plots out the results of the sub-scheme. As seen from the plots, the errors of the combined weighted measurements were much lower at different altitudes, and thus this combined measurement was proven to be reliable.

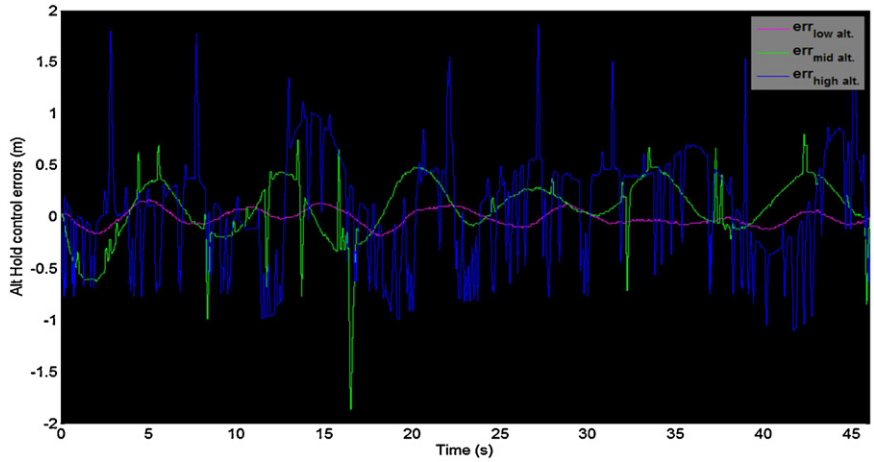

Fig. 13. Altitude errors for ultrasonic sensor in altitude control.

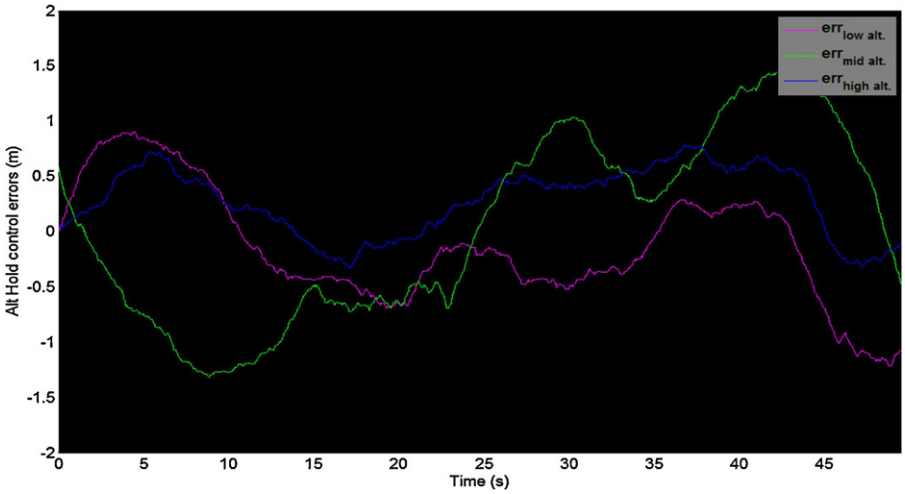

Fig. 14. Altitude errors for pressure sensor in altitude control.

At lower altitudes, this fusion sub-scheme took in a more heavily weighted ultrasonic sensor measurement, which was reliable, as seen from Fig. 15. Therefore, it was able to track and regulate the altitude error well, because the standard deviation at lower altitudes was only about 0.07 m. At mid altitudes, even though there was an increase in noise in the ultrasonic sensor measurements, this scheme was able to utilize the less noisy barometer readings to attenuate the noise partially. The standard deviation of the altitude error at mid altitudes was 0.201 m. At higher altitudes, the pressure sensor measurements were weighted more heavily, and at the same time the noisy ultrasonic sensor readings were weighted to a lesser extent as their reliability decreased. This allowed the altitude error to remain quite small in magnitude and have a standard deviation of 0.259 m. Therefore, through observations from flight tests and analysis of this logged information, it could be seen that the altitude estimation and control algorithm allowed the platform to track and control its altitude well at varying altitudes by combining readings from both sensors.

For the altitude controller, different sets of gains were required at different altitudes, based on the sensors that were used. This can be seen as a simplified form of gain scheduling, with the altitude as the scheduling parameter for the controller.

4.3. Autonomous navigation results

Before performing the autonomous navigation scheme, it is necessary for the platform to obtain a good position estimate and to loiter in a desired location reasonably well. For loitering tests, the coordinates (latitude and longitude) of the platform were logged during the flight tests and was imported to MATLAB and Google Earth for post processing and trajectory plotting. These loitering flights were conducted in an enclosed outdoor test-bed where the GPS device could provide sufficient information for the position estimate. Fig. 16 shows one of the tests to verify the loitering capabilities of the platform.

As seen in Fig. 16, the pilot was not controlling the UAV (highlighted in red) via the transmitter (highlighted in yellow), and the UAV was able to maintain its position well. The results of one of the position hold tests are shown in Fig. 17. In this figure, the latitude and longitude were extracted and a two-dimensional trajectory was plotted, highlighted in blue.

As shown in the figure, the platform was able to maintain its position well, within a circle of 5 m radius (highlighted in orange), noting that the resolution of most GPS devices is about 3 to 5 m. To be able to hold its position within such limits was sufficient for it to perform other navigation related tasks.

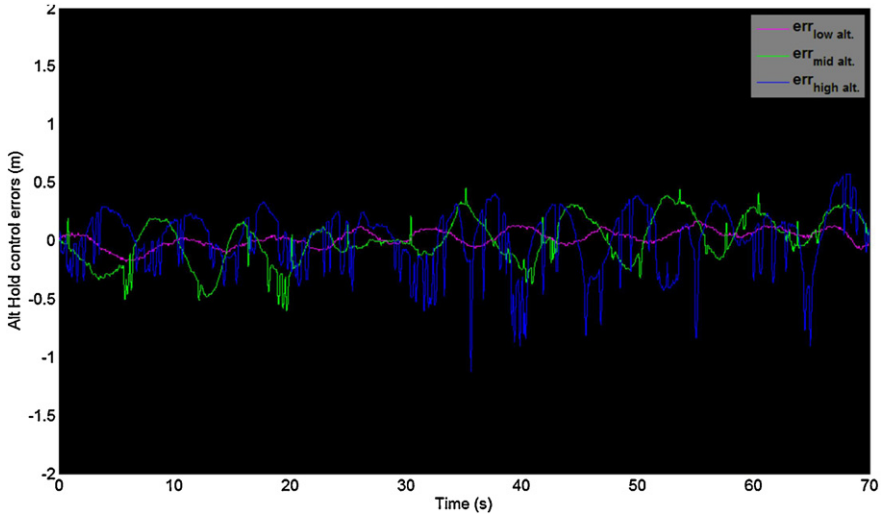

Fig. 15. Altitude errors for combined measurements in altitude control.

Fig. 16. Flight test for loitering and position estimation, without pilot intervention.

Fig. 17. Trajectory of vehicle during loitering.

Next, the autonomous navigation scheme was tested on the same outdoor environment. Two waypoints (WPs) were defined by the pilot prior to flight. The trajectory of one of the flights with two waypoints is shown in Fig. 18. The trajectory of the UAV is highlighted in blue. The starting position of the UAV and waypoints are also shown. At the starting position, the GPS unit was initialized and calibrated to ensure good accuracy of its performance. Next, it was flown in the stabilization and altitude hold mode, before transiting into the waypoint navigation mode. As shown in the figure, the UAV was able to travel to the waypoints in a reasonable manner. The cross track error found in some parts of the trajectory plotted could be due to the inaccuracy of the position estimate given by the GPS device or due to gust disturbances affecting the operation of the UAV during flight. In general, the deviation from the target path was small. The distance between the two waypoints was set at approximately 26 m.

Fig. 18. Autonomous waypoint navigation with two waypoints.

Fig. 19. Autonomous waypoint navigation with four waypoints.

Another waypoint navigation test was done with two additional waypoints, in the same test environment. The results of these tests are shown in Fig. 19. Throughout this navigation scheme, roll, pitch and yaw commands were given to allow the UAV to move towards the next waypoint via the shortest distance possible. Also, the platform was commanded to loiter at each of the waypoints for about five seconds before moving onto the next waypoint. As shown in the figure, the quadrotor platform was able to track a path governed by four waypoints reasonably well. Cross-track error during motion was also minimal, thus proving the efficiency of this guidance algorithm.

4.4. Collision avoidance results

The next series of flight tests for the verification of the collision avoidance algorithms were performed in a similar outdoor test-bed. To verify the reliability of the IR sensors and the algorithm, objects of different materials such as wood and human-like obstacles were used to test if common objects found in a practical urban environment would trigger detection from the sensors. One of these tests is illustrated in Fig. 20. As shown in the figure, a wooden obstacle, highlighted in orange, was used for this test. The flight tests were performed at altitudes ranging from 1 to 3 metres, at which these urban objects could be imposed on the platform. The detection of the obstacles occurs when the object is approximately 1.5 metres in the vicinity of the platform. This is due to the maximum range of the sensors used. Thus, this range can be extended, if other rangefinders are utilized.

Results for the reactive quad-directional algorithm can be illustrated using Fig. 21, and they demonstrate the fact that the UAV was avoiding obstacles without any pilot inputs. In this figure, the blue plot gives the estimated attitude of the vehicle. The red plot is the radio input by the pilot. These plots are normalized and scaled for better comparison with the other plots in the same figure. Some of these radio inputs are circled in magenta for clarity. The plot in green is the attitude command given to the platform when the IR sensors detect an obstacle. They are given by the differential

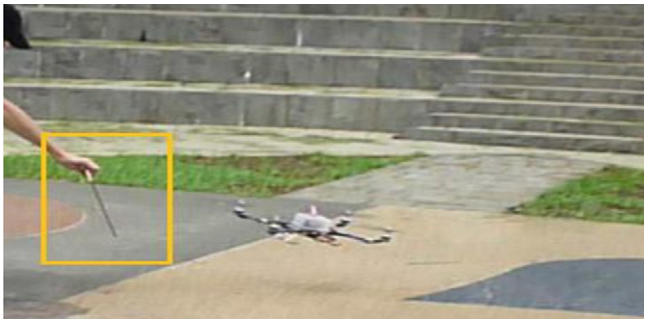

Fig. 20. Verification of the collision detection and avoidance algorithm.

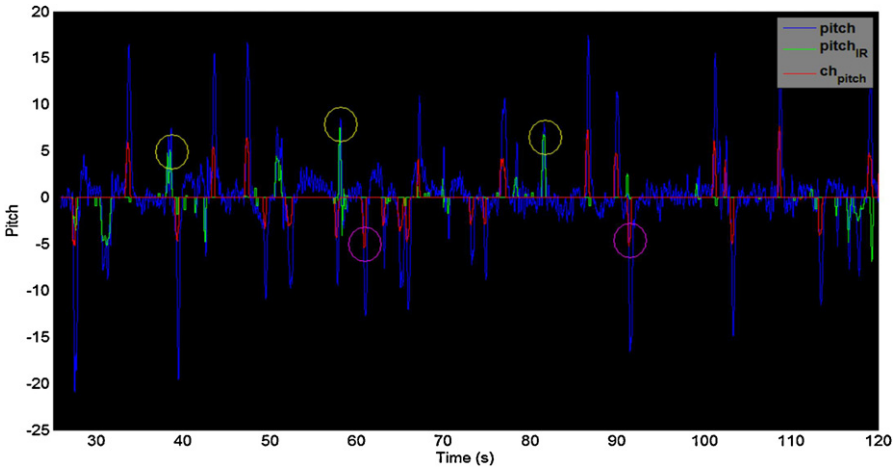

Fig. 21. Attitude parameters for reactive collision avoidance scheme.

measurements of the IR sensors mounted on the platform. For the pitch command, it is a scaled version of the difference in measurements between the front and back IR sensors. These differential measurements were then used to compute errors which were fed back into the controllers in order to regulate them to zero. Some of these IR measurement plots are circled in yellow for clarity. Therefore, this plot illustrates the capability of the collision avoidance algorithm.

Next, for the combinational flight mode of autonomous navigation and collision avoidance, tests were conducted without pilot intervention and in a suitable enclosed outdoor test environment. The vehicle was first set to the altitude control mode straight after take-off and allowed to maintain a reasonable height, ranging from 1 to 3 meters so that the waypoint navigation and collision avoidance schemes could be performed. After that, the navigational collision avoidance algorithm was toggled and the UAV autonomously moved to the waypoints and avoided any obstacle presented to it as it navigated within the flight zone. Fig. 22 shows a picture where the platform (highlighted in red) was navigating to its next waypoint, while performing collision avoidance

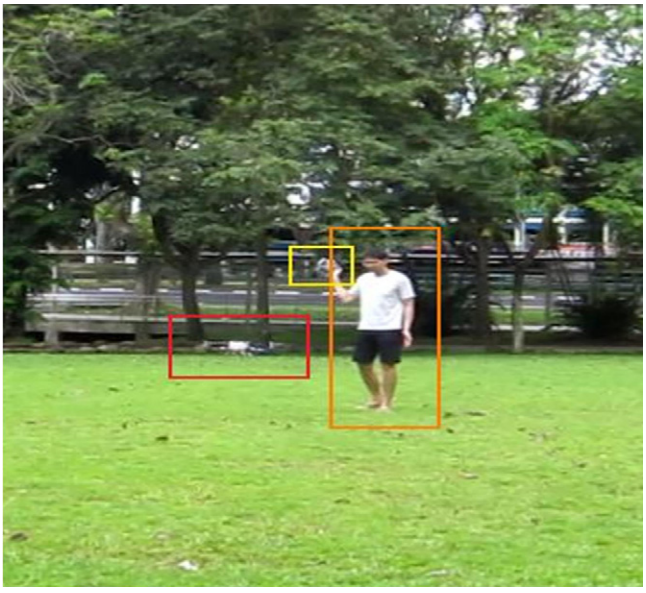

Fig. 22. Flight test for combinational mode of waypoint navigation and collision avoidance.

Fig. 23. Trajectory of the UAV during navigation and collision avoidance.

commands, with the urban obstacle in its path (highlighted in orange) and without any pilot intervention (highlighted in yellow).

Next, for the combinational flight mode of autonomous navigation and collision avoidance, flight information such as the radio inputs, measurements given by the ultrasonic and infra-red sensors as well as attitude and position information was logged and post processed in MATLAB and plotted in Google Earth to show and demonstrate the feasibility and capability of the algorithm.

Fig. 23 depicts the trajectory taken by the vehicle when it was navigating for one point to another and when it met an obstacle along its flight path. As shown in the figure, the vehicle was able to maneuver itself away from the obstacle presented in front of it and moved backward and sideward in order to avoid the obstacle and implemented an alternative flight path. With this ability to avoid obstacles of unknown shape and size, the vehicle would be able to avoid bigger obstacles such as buildings and ground vehicles, and thus this scheme can potentially improve the mission capability and autonomy of the UAV in urban terrains where the presence of obstacles is inevitable and has to be avoided at all costs in order to perform the missions successfully.

5. Conclusion

This paper elaborates on the development of a quadrotor platform that is able of performing attitude estimation and stabilization using an onboard flight processor and an AHRS module. It has demonstrated practical mission capabilities such as altitude control, autonomous navigation and collision avoidance, through the implementation of various algorithms discussed in Section 3. Future work includes the addition of external sensors such as a laser range finder, which can be used to map unknown terrains

and improve the navigation capability of the platform. Further flight tests can also be performed to investigate the effects of the collision avoidance algorithms on larger obstacles such as urban infrastructure and ground vehicles.

References

[1] P. Pounds, R., Mahony, J. Gresham, Towards dynamically-favourable quad-rotor aerial robots http://eprints.qut.edu.au/33833/1/33833.pdf (Last accessed on 18 May 2012).

[2] G.M. Hoffmann, H. Huang, S.L. Waslander, C.J. Tomlin, Quadrotor helicopter flight dynamics and control: Theory and experiment, in: Proceedings of AIAA Guidance, Navigation and Control Conference and Exhibit, August 20–23, Hilton Head, South Carolina, 2007, pp. 1670–1689.

[3] T. Bresciani, Modeling, identification and control of a quadrotor helicopter, M.Sc. thesis, Lund University, Sweden. 2008.

[4] G. Wei, J.F. Horn, Modeling and simulation for the development of a Quad-Rotor UAV capable of indoor flight, in: Proceedings of AIAA Modeling and Simulation Technologies Conference and Exhibit, August 21–24, Keystone, Colorado, 2006, pp. 1117–1127.

[5] S. Bouabdallah, A. Noth, R. Siegwart, PID vs LQ control techniques applied to an indoor micro Quadrotor, in: Proceedings of IEEE/RSJ International Conference on Intelligent Robots and Systems, Sept 28–Oct 2, Sendal, Japan, 2004, pp. 2451–2456.

[6] B. Erginer, E. Altug, Modeling and PID control of a quadrotor VTOL vehicle, IEEE Intelligent Vehicles Symposium, March 13–15, Istanbul, Turkey, 2007.

[7] Z.T. Dydek, A.M., Annaswamy, E. Lavretsky, Adaptive control of quadrotor UAVS in the presence of actuator uncertainties, AIAA Infotech@Aerospace, April 20–22, Atlanta, Georgia, 2010.

[8] A.A. Mian, D. Wang, Modeling and backstepping-based nonlinear control strategy for a 6 DOF quadrotor helicopter, Chinese Journal of Aeronautics 21 (2008) 261–268.

[9] F. Kendoul, D. Lara, I. Fantoni, R. Lozano, Nonlinear control for systems with bounded inputs: Real-time embedded control applied to UAVs, in: Proceedings of 45th IEEE Conference on Decision and Control, December 13 -15, San Diego, CA, USA, 2006, pp. 5888–5893.

[10] I.F. Mondragón, M.A. Olivares-Méndez, P. Campoy, C. Martínez, L. Mejias, Unmanned aerial vehicles UAVs attitude, height, motion estimation and control using visual systems, Autonomous Robots 29 (2010) 17–34.

[11] M.G. Earl, R. D'Andrea, Real-time attitude estimation techniques applied to a four rotor helicopter, in: Proceedings of 43rd IEEE Conference on Decision and Control, December 14 - 17, Atlantis, Paradise Island, Bahamas, 2004, pp. 3956–3961.

[12] S.K. Hong, Fuzzy logic based closed-loop strapdown attitude system for unmanned aerial vehicle (UAV), Sensors and Actuators A: Physical 107 (2003) 109–118.

[13] J. Stowers, M. Hayes, A. Bainbridge-Smith, Altitude control of a quadrotor helicopter using depth map from Microsoft Kinect sensor, in: Proceedings of IEEE International Conference on Mechatronics, April 13–15, Istanbul, Turkey, 2011, pp. 358–362.

[14] J.F. Roberts, T.S., Stirling, J., Zufferey, D. Floreano, Quadrotor using minimal sensing for autonomous indoor flight, European Micro Air Vehicle Conference and Flight Competition, 17-21 September, Toulouse, France, 2007.

[15] S. Grzonka, G. Grisetti, W. Burgard, A fully autonomous indoor quadrotor, IEEE Transactions on Robotics 28 (2012) 90–100.

[16] M. Achtelik, A., Bachrach, R., He, S., Prentice, N. Roy, Autonomous Navigation and Exploration of a Quadrotor Helicopter in GPS-denied Indoor Environments, Robotics: Science and Systems Conference, June 27-30, Atlanta, Georgia, 2008.

[17] J. Kim, G. Brambley, Dual optic-flow integrated navigation for small-scale flying robots, Australasian Conference on Robotics and Automation, December 10 -12, Brisbane, Australia, 2007.

[18] B. Sinopoli, M. Micheli, G. Donato, T.J. Koo, Vision based navigation for an unmanned aerial vehicle, in: Proceedings of IEEE International Conference on Robotics and Automation, My 21- 26, Seoul, Korea, 2001, pp. 1757–1764.

[19] A. Rodić, G. Mester, The modeling and simulation of an autonomous quad-rotor microcopter in a virtual outdoor scenario, Acta Polytechnica Hungarica 8 (2011) 107–122.

[20] T. Puls, M. Kemper, R. Küke, A. Hein, GPS-based position control and waypoint navigation system for quadrocopters, in: Proceedings of IEEE/RSJ International Conference on Intelligent Robots and Systems, October 11-15, St, Louis, USA, 2009, pp. 3374–3379.

[21] R. Mahony, T. Hamel, J.M. Pflimlin, Nonlinear complementary filters on the special orthogonal group, IEEE Transactions on Automatic Control 53 (2008) 1203–1218.

[22] Arducopter, Arducopter Project, Version 2.1 http://code.google.com/p/arducopter/(Last accessed on 25 Dec 2011).

Biographies

K.Y. Chee received his Bachelor of Engineering in Mechanical and Aerospace Engineering (Honour) from Nanyang Technological University in 2012.

Z.W. Zhong worked at the Institute of Physical and Chemical Research, Japan after he received his Doctor of Engineering in Precision Engineering in 1989. He has also worked at the Gintic Institute of Manufacturing Technology, Singapore, and is currently at the Nanyang Technological University, Singapore. His research and development areas are precision engineering, mechatronics and design.